International Journal of Modern Physics C, Vol. 13, No. 10 (2002) 1399–1414

SIMULATION OF NATURAL CONVECTION IN A SQUARE CAVITY BY TAYLOR SERIES EXPANSION- AND LEAST SQUARES-BASED LATTICE BOLTZMANN METHOD

C. SHU, Y. PENG and Y. T. CHEW

Department of Mechanical Engineering, National University of Singapore
10 Kent Ridge Crescent, Singapore 119260

Received 23 April 2002
Revised 4 June 2002

The Taylor series expansion- and least squares-based lattice Boltzmann method (TLLBM) was used in this paper to extend the current thermal model to an arbitrary geometry so that it can be used to solve practical thermo-hydrodynamics in the incompressible limit. The new explicit method is based on the standard lattice Boltzmann method (LBM), Taylor series expansion and the least squares approach. The final formulation is an algebraic form and essentially has no limitation on the mesh structure and lattice model. Numerical simulations of natural convection in a square cavity on both uniform and nonuniform grids have been carried out. Favorable results were obtained and compared well with the benchmark data. It was found that, to get the same order of accuracy, the number of mesh points used on the nonuniform grid is much less than that used on the uniform grid.

Keywords: Lattice Boltzmann method; algebraic formulation; Taylor series expansion; least squares; internal energy density distribution function; natural convection.

1. Introduction

In the past ten years, the LBM has been developed into an alternative approach for solving complex fluid dynamic problems. However, because of the essential restriction of the standard LBM to the lattice-uniformity, the broad application of the LBM in engineering has been greatly hampered. For many practical problems, an irregular grid or a meshless structure is always preferable due to the fact that curved boundaries can be described more accurately, and that computational resources can be used more efficiently with it. Even when the physical domain is regular, a nonuniform grid is needed when solving flow problems with high Reynolds or Rayleigh number, where the boundary layer is very thin. In order to capture the physical properties within the boundary layer, a lot of grid points are needed on the uniform grid. This wastes a lot of computational time when such a fine grid is also used in the smooth flow region. An effective way to solve the above problem is to use a mesh with a clustering of grid points in critical regions, which is a convenient way used in conventional CFD methods.

Currently, there are two ways to improve the standard LBM so that it can be applied to complex problems. One is the interpolation-supplemented LBM (ISLBM) proposed by He and his colleagues.[1–3] The other is based on the solution of a differential lattice Boltzmann equation (LBE). For complex problems, the differential LBE can be solved by the finite difference (FDLBE) method with the help of coordinate transformation[4] or by the finite volume (FVLBE) approach.[5–7] Numerical experiences have shown that these methods have good capability in real applications. However, the ISLBM has an extra computational effort for interpolation at every time step, and also has a strict restriction on the selection of the interpolation points, which requires upwind nine points for two-dimensional problems and upwind twenty-seven points for three-dimensional problems if a structured mesh is used. For the FDLBE and FVLBE methods, one needs to select efficient approaches such as upwind schemes to do numerical discretization in order to get the stable solution. As a consequence, the computational efficiency greatly depends on the selected numerical scheme. In addition, the numerical diffusion may affect the accuracy of the results, especially in the region where the flow gradient is large.[8]

In order to implement the LBM more efficiently for flows with arbitrary geometry, the TLLBM, which is based on the standard lattice Boltzmann method (LBM), Taylor series expansion and the least squares approach, was proposed by Shu *et al.*[9] The final form is an algebraic formulation, in which the coefficients depend only on the coordinates of the mesh points and the lattice velocity, and can be computed once in advance. This new method can be consistently used in any kind of lattice model. Numerical experiments on isothermal flows show that this method is an efficient and flexible approach for practical application.

For the thermal flow problems, besides the above-mentioned lattice-uniformity restriction as in the isothermal flow and due to complexity of the thermal problem itself, the current thermal LBM is restricted to the regular grid, which limits its application. In order to solve this problem, the current thermal model is extended in this work for its application on an arbitrary mesh using the above-mentioned techniques. Numerical simulations of natural convection in a square cavity on both uniform and nonuniform grids were carried out. The numerical results agree very well with the benchmark data. This indicates that the TLLBM can be used to extend the current thermal model to solve the complex thermal flow problem. The comparison of the numerical results on uniform and nonuniform grids showed that on nonuniform grids, the use of fewer grid points could also give very accurate numerical results.

2. Methodology

2.1. *Taylor series expansion- and least squares-based LBM (TLLBM)*

The TLLBM is based on the well-known fact that the distribution function is a continuous function in physical space and can be well defined in any mesh system.

The details of TLLBM can be found in Ref. 9. Some basic description of TLLBM is shown below.

The two-dimensional, standard LBE with BGK approximation can be written as

$$f_\alpha(x + e_{\alpha x}\delta t, y + e_{\alpha y}\delta t, t + \delta t) = f_\alpha(x, y, t) + \frac{f_\alpha^{\mathrm{eq}}(x, y, t) - f_\alpha(x, y, t)}{\tau}\,,$$
$$\alpha = 0, 1, \ldots, N\,, \tag{1}$$

where τ is the single relaxation time; f_α is the distribution function along the α direction; f_α^{eq} is its corresponding equilibrium state; δt is the time step and $\mathbf{e}_\alpha(e_{\alpha x}, e_{\alpha y})$ is the particle velocity in the α direction; N is the number of discrete particle velocities. Obviously, the standard LBE consists of two steps: collision and streaming. The macroscopic density ρ and momentum density $\rho\mathbf{V}$ are defined as

$$\rho = \sum_{\alpha=0}^{N} f_\alpha\,, \quad \rho\mathbf{V} = \sum_{\alpha=0}^{N} f_\alpha \mathbf{e}_\alpha\,. \tag{2}$$

Suppose that a particle is initially at the grid point (x, y, t). Along the α direction, this particle will stream to the position $(x + e_{\alpha x}\delta t, y + e_{\alpha y}\delta t, t + \delta t)$. For a uniform lattice, $\delta x = e_{\alpha x}\delta t$, $\delta y = e_{\alpha y}\delta t$. So, $(x + e_{\alpha x}\delta t, y + e_{\alpha y}\delta t)$ is on the grid point. In other words, Eq. (1) can be used to update the distribution functions exactly at the grid points. However, for a nonuniform grid, $(x + e_{\alpha x}\delta t, y + e_{\alpha y}\delta t)$ is usually not at the grid point $(x + \delta x, y + \delta y)$. In the numerical simulation, only the distribution function at the mesh points for all the time levels are needed, so that the macroscopic properties such as the density, flow velocity and temperature can be evaluated at every mesh point. To get the distribution function at the grid point $(x + \delta x, y + \delta y)$ and the time level $t + \delta t$, the Taylor series expansion in the spatial direction is applied.

As shown in Fig. 1, for simplicity, the point A represents the grid point (x_A, y_A, t), point A' represents the position $(x_A + e_{\alpha x}\delta t, y_A + e_{\alpha y}\delta t, t + \delta t)$, and

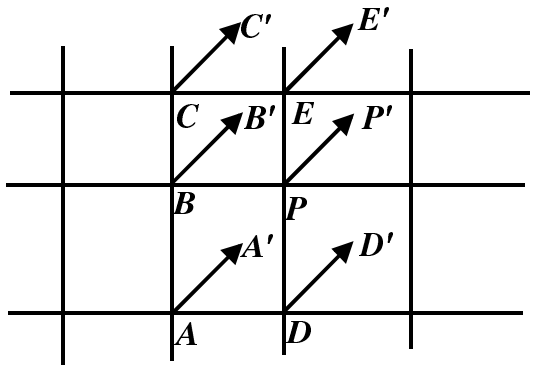

Fig. 1. Configuration of particle movement along the α Direction.

point P represents the position $(x_P, y_P, t+\delta t)$ with $x_P = x_A + \delta x$, $y_P = y_A + \delta y$. So, Eq. (1) gives

$$f_\alpha(A', t+\delta t) = f_\alpha(A,t) + \frac{[f_\alpha^{\mathrm{eq}}(A,t) - f_\alpha(A,t)]}{\tau}\,. \tag{3}$$

For the general case, A' may not coincide with the mesh point P. We truncate the Taylor series expansion to the second order derivative terms. So $f_\alpha(A', t+\delta t)$ can be approximated by the corresponding function and its derivatives at the mesh point P as

$$\begin{aligned} f_\alpha(A', t+\delta t) = {} & f_\alpha(P, t+\delta t) + \Delta x_A \frac{\partial f_\alpha(P, t+\delta t)}{\partial x} + \Delta y_A \frac{\partial f_\alpha(P, t+\delta t)}{\partial y} \\ & + \frac{1}{2}(\Delta x_A)^2 \frac{\partial^2 f_\alpha(P, t+\delta t)}{\partial x^2} + \frac{1}{2}(\Delta y_A)^2 \frac{\partial^2 f_\alpha(P, t+\delta t)}{\partial y^2} \\ & + \Delta x_A \Delta y_A \frac{\partial^2 f_\alpha(P, t+\delta t)}{\partial x \partial y} + O[(\Delta x_A)^3, (\Delta y_A)^3]\,, \end{aligned} \tag{4}$$

where $\Delta x_A = x_A + e_{\alpha x}\delta t - x_P$, $\Delta y_A = y_A + e_{\alpha y}\delta t - y_P$. For the two-dimensional case, this expansion involves six unknowns, that is, one distribution function at the time level $t+\delta t$, two first-order derivatives, and three second-order derivatives. To solve for these unknowns, six equations are needed to close the system. This can be done by applying the second-order Taylor series expansion at six points: P, A, B, C, D, E. The following equation system can be obtained

$$f_i' = \{s_i\}^T \{W\} = \sum_{j=1}^{6} s_{i,j} W_j\,, \quad i = P, A, B, C, D, E \tag{5}$$

where

$$f_i' = f_\alpha(x_i, y_i, t) + \frac{[f_\alpha^{\mathrm{eq}}(x_i, y_i, t) - f_\alpha(x_i, y_i, t)]}{\tau}$$

$$\{s_i\}^T = \left\{1, \Delta x_i, \Delta y_i, \frac{(\Delta x_i)^2}{2}, \frac{(\Delta y_i)^2}{2}, \Delta x_i \Delta y_i\right\}$$

$$\{W\} = \left\{f_\alpha, \frac{\partial f_\alpha}{\partial x}, \frac{\partial f_\alpha}{\partial y}, \frac{\partial^2 f_\alpha}{\partial x^2}, \frac{\partial^2 f_\alpha}{\partial^2 y}, \frac{\partial^2 f_\alpha}{\partial x \partial y}\right\}^T .$$

Our target is to find its first element $W_1 = f_\alpha(P, t+\delta t)$. Equation (5) can be put into the following matrix form

$$[S]\{W\} = \{f'\}\,. \tag{6}$$

In practical applications, it was found that the matrix $[S]$ might be singular or ill conditioned. To overcome this difficulty and make the method be more general, the least squares approach was introduced to optimize the approximation by Eq. (6). As a result, the equation system for $\{W\}$ becomes

$$\{W\} = ([S]^T[S])^{-1}[S]^T\{f'\} = [A]\{f'\}\,. \tag{7}$$

From Eq. (7), we can have

$$f_\alpha(x_0, y_0, t + \delta t) = W_1 = \sum_{k=1}^{M+1} a_{1,k} f'_{k-1}\,, \tag{8}$$

where $a_{1,k}$ are the elements of the first row of the matrix $[A]$, which is determined by the coordinates of mesh points, the particle velocity and time step size, and will not be changed in the calculation procedure. We can calculate once and store in advance, so little computational effort is introduced as compared with the standard LBE. On the other hand, Eq. (8) is nothing to do with the mesh structure. It needs only the information of coordinates of the mesh points. Thus, we can say that Eq. (8) can be consistently used for any kind of mesh structure.

2.2. *The IEDDF thermal model and its extension to arbitrary mesh system by using TLLBM*

The LBM still has some difficulties in the simulation of thermo-hydrodynamics in contrast to its successful applications to isothermal flows. One of the thermal models was introduced by Alexander,[10] which used only the density distribution function, a small number of discrete velocity states and a linear single-time relaxation collision operator. The local equilibrium distribution included the higher order velocity terms $\mathbf{V}$. But this model was restricted to flows with fixed Prandtl number of 0.5. The succeeding thermal models fall into three categories: the multispeed model,[11,12] the passive-scalar thermal model[13] and the internal energy density distribution function (IEDDF) model proposed by He.[14] In the multispeed model, the additional speeds are necessary and the equilibrium distribution must include the higher order velocity terms; while the passive-scalar model utilizes the fact that the macroscopic temperature satisfies the same evolution equation as a passive scalar. The IEDDF model has proven itself to be a stable and simple thermal model. So this model is used in this paper. In the year 2000, a thermal model for nonideal gases with potential energy was presented by Ihle.[15] In addition to the single particle distribution function, additional distribution functions for the potential energy and the nonideal part of the pressure tensor are also defined which contain information about the two-particle distribution functions.

The IEDDF model introduces an internal energy density distribution function to simulate the temperature field. The macroscopic density and velocity fields are still simulated using the density distribution function.

The density distribution function and energy density distribution function satisfy the following equations respectively:

$$\partial_t f + (\mathbf{e}\cdot\nabla) f = -\frac{f - f^{\mathrm{eq}}}{\tau_\nu} + F\,, \tag{9}$$

$$\partial_t g + (\mathbf{e}\cdot\nabla) g = -\frac{g - g^{\mathrm{eq}}}{\tau_c} - f(\mathbf{e} - \mathbf{V})\cdot[\partial_t \mathbf{V} + (\mathbf{e}\cdot\nabla)\mathbf{V}]\,, \tag{10}$$

where $F = ((\mathbf{G}\cdot(\mathbf{e}-\mathbf{V}))/RT)f^{\mathrm{eq}}$, and $\mathbf{G}$ is the external force acting on the unit mass. By adopting a second-order integration to above two equations, we can get

$$\bar{f}_\alpha(x+e_\alpha\delta t, t+\delta t) - \bar{f}_\alpha(x,t) = -\frac{\delta t}{\tau_\nu + 0.5\delta t}[\bar{f}_\alpha(x,t) - f_\alpha^{\mathrm{eq}}(x,t)] + \frac{\tau_\nu F_\alpha \delta t}{\tau_\nu + 0.5\delta t}, \tag{11}$$

$$\bar{g}_\alpha(x+e_\alpha\delta t, e, t+\delta t) - \bar{g}_\alpha(x,e_\alpha,t) = -\frac{\delta t}{\tau_c + 0.5\delta t}[\bar{g}_\alpha(x,e_\alpha,t) - g_\alpha^{\mathrm{eq}}(x,e_\alpha,t)] - \frac{\tau_c}{\tau_c+0.5\delta t} f_\alpha(x,e_\alpha,t) q(x,e_\alpha,t)\delta t, \tag{12}$$

where

$$\bar{f}_\alpha = f_\alpha + \frac{\delta t}{2\tau_\nu}(f_\alpha - f_\alpha^{\mathrm{eq}}) - \frac{\delta t}{2}F_\alpha,$$

$$\bar{g}_\alpha = g_\alpha + \frac{\delta t}{2\tau_c}(g_\alpha - g_\alpha^{\mathrm{eq}}) + \frac{\delta t}{2} f_\alpha q_\alpha,$$

$$f_\alpha = \frac{\tau_\nu \bar{f}_\alpha + 0.5\delta t f_\alpha^{\mathrm{eq}} + 0.5\delta t \tau_\nu F_\alpha}{\tau_\nu + 0.5\delta t},$$

$$q_\alpha = (\mathbf{e}_\alpha - \mathbf{V})\cdot\left[\frac{1}{\rho}(-\nabla p + \nabla\cdot\Pi) + (\mathbf{e}_\alpha - \mathbf{V})\cdot\nabla\mathbf{V}\right],$$

$$F_\alpha = \frac{\mathbf{G}\cdot(\mathbf{e}_\alpha - \mathbf{V})}{RT} f_\alpha^{\mathrm{eq}}.$$

When the nine-bit model is used, which is defined as

$$\mathbf{e}_\alpha = \begin{cases} 0 & \alpha = 0 \\ \left(\cos\left[\dfrac{(\alpha-1)\pi}{2}\right], \quad \sin\left[\dfrac{(\alpha-1)\pi}{2}\right]\right)c & \alpha = 1,2,3,4 \\ \sqrt{2}\left(\cos\left[\dfrac{(\alpha-5)\pi}{2}+\dfrac{\pi}{4}\right], \quad \sin\left[\dfrac{(\alpha-5)\pi}{2}+\dfrac{\pi}{4}\right]\right)c & \alpha = 5,6,7,8 \end{cases} \tag{13}$$

where $c = \sqrt{3RT}$, the equilibrium functions for the density and energy density distribution functions are given as

$$f_\alpha^{\mathrm{eq}} = w_\alpha \rho\left[1 + \frac{3\mathbf{e}_\alpha\cdot\mathbf{V}}{c^2} + \frac{9(\mathbf{e}_\alpha\cdot\mathbf{V})^2}{2c^4} - \frac{3\mathbf{V}^2}{2c^2}\right], \tag{14}$$

where $w_0 = 4/9$, $w_\alpha = 1/9$ for $\alpha = 1, 2, 3, 4$, $w_\alpha = 1/36$ for $\alpha = 5, 6, 7, 8$

$$g_0^{\mathrm{eq}} = -\frac{2\rho\varepsilon}{3}\frac{\mathbf{V}^2}{c^2}, \tag{15a}$$

$$g_{1,2,3,4}^{\mathrm{eq}} = \frac{\rho\varepsilon}{9}\left[1.5 + 1.5\frac{\mathbf{e}_\alpha\cdot\mathbf{V}}{c^2} + 4.5\frac{(\mathbf{e}_\alpha\cdot\mathbf{V})^2}{c^4} - 1.5\frac{\mathbf{V}^2}{c^2}\right], \tag{15b}$$

$$g^{\mathrm{eq}}_{5,6,7,8} = \frac{\rho\varepsilon}{36}\left[3 + 6\frac{\mathbf{e}_\alpha \cdot \mathbf{V}}{c^2} + 4.5\frac{(\mathbf{e}_\alpha \cdot \mathbf{V})^2}{c^4} - 1.5\frac{\mathbf{V}^2}{c^2}\right]. \tag{15c}$$

Then the macroscopic density, velocity and temperature are calculated by

$$\rho = \sum_\alpha \bar{f}_\alpha\,, \tag{16a}$$

$$\rho\mathbf{V} = \sum_\alpha \mathbf{e}_\alpha \bar{f}_\alpha + \frac{\rho\mathbf{G}\delta t}{2}\,, \tag{16b}$$

$$\rho\varepsilon = \sum_\alpha \bar{g}_\alpha - \frac{\delta t}{2}\sum_\alpha f_\alpha q_\alpha\,. \tag{16c}$$

The kinetic viscosity and the thermal conductivity are defined as

$$\upsilon = \tau_\nu RT \quad \alpha = 2\tau_c RT\,. \tag{17}$$

When Eqs. (11) and (12) are used on an arbitrary mesh, $(x + e_{\alpha x}\delta t, y + e_{\alpha y}\delta t)$ is usually not at the grid point $(x + \delta x, y + \delta y)$. To solve this problem, the TLLBM technique can be applied to Eqs. (11) and (12) following the same procedure as shown in the previous section for the isothermal flow, which results in

$$\bar{f}_\alpha(x_0, y_0, t + \delta t) = W_1 = \sum_{k=1}^{M+1} a_{1,k}\bar{f}'_{k-1}\,, \tag{18}$$

$$\bar{g}_\alpha(x_0, y_0, t + \delta t) = W'_1 = \sum_{k=1}^{M+1} a'_{1,k}\bar{g}'_{k-1}\,, \tag{19}$$

where

$$\begin{aligned}
\bar{f}'_k &= \left(1 - \frac{\delta t}{\tau_\nu + 0.5\delta t}\right) f_\alpha(x_k, y_k, e_\alpha, t) \\
&\quad + \frac{\delta t}{\tau_\nu + 0.5\delta t} f^{\mathrm{eq}}_\alpha(x_k, y_k, e_\alpha, t) + \frac{\tau_\nu F_\alpha \delta t}{\tau_v + 0.5\delta t}\,, \\
\bar{g}'_k &= \left(1 - \frac{\delta t}{\tau_c + 0.5\delta t}\right) g_\alpha(x_k, y_k, e_\alpha, t) \\
&\quad + \frac{\delta t}{\tau_c + 0.5\delta t} g^{\mathrm{eq}}_\alpha(x_k, y_k, e_\alpha, t) - \frac{\tau_c f_\alpha q_\alpha \delta t}{\tau_c + 0.5\delta t}\,, \\
\{W'\} &= \left\{g_\alpha, \frac{\partial g_\alpha}{\partial x}, \frac{\partial g_\alpha}{\partial y}, \frac{\partial^2 g_\alpha}{\partial x^2}, \frac{\partial^2 g_\alpha}{\partial^2 y}, \frac{\partial^2 g_\alpha}{\partial x \partial y}\right\}^T.
\end{aligned}$$

When the same particle velocity model is chosen for the density and energy density distribution functions, the geometric matrix A and A' are the same, which can save both computational time and storage space.

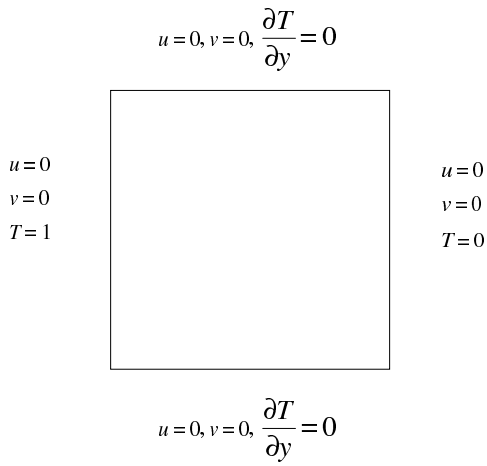

Fig. 2. Configuration of natural convection in a square cavity.

3. Numerical Simulation

In order to verify whether the TLLBM can be used to solve the thermal problem on the arbitrary mesh, we carried out the computation for a sample problem. The problem considered is a natural convection in a two-dimensional square cavity with sidewalls maintained at different temperatures. The temperature difference between the walls introduces a temperature gradient in a fluid, and the consequent density difference induces a fluid motion, that is, convection. The top and bottom walls are adiabatic. The problem definition and the boundary conditions are displayed in Fig. 2.

3.1. *Buoyancy force and dimensionless parameter*

The Boussinesq approximation is applied to the buoyancy force term. This means that the properties β and υ are considered as constants, the density ρ is constant, and the buoyancy term is assumed to depend linearly on the temperature,

$$\rho \mathbf{G} = \rho \beta g_0 (T - T_m) j \,, \tag{20}$$

where β is the thermal expansion coefficient, g_0 is the acceleration due to gravity, T_m is the average temperature, and j is the vertical direction opposite to that of gravity.

The dynamical similarity depends on two dimensionless parameters: Prandtl number Pr and Rayleigh number Ra,

$$\mathrm{Pr} = \frac{\upsilon}{\alpha} \quad \mathrm{Ra} = \beta g_0 \frac{\Delta T L^3}{\upsilon \alpha} \,.$$

To ensure the code is working properly in the near-incompressible regime, we carefully choose the value of $\beta g_0 \Delta T L$. Once $\beta g_0 \Delta T L$ is determined, the kinetic viscosity

and the thermal conductivity are determined through the two dimensionless numbers, Pr and Ra respectively. By using Eq. (17), two relaxation time τ_ν, τ_c are determined. Nusselt number Nu is one of the most important dimensionless parameters in describing the convective heat transport. Its average in the whole flow domain and along the vertical line of $x = x_0$ can be defined by

$$\overline{\mathrm{Nu}} = \frac{H}{\alpha \Delta T} \frac{1}{H^2} \int_0^H \int_0^H q_z(x, z) dx dz \,, \tag{21}$$

$$\mathrm{Nu} = \frac{H}{\alpha \Delta T} \frac{1}{H} \int_0^H q_z(x_0, z) dz \,, \tag{22}$$

where $q_z(x, z) = uT(x, z) - \alpha(\partial/\partial x)T(x, z)$ is the local heat flux in horizontal direction.

3.2. *Implementation of boundary condition*

The implementation of boundary condition is very important in the simulation. The unknown distribution functions pointing to the fluid field at the boundary node must be specified. The bounce-back rule of the nonequilibrium distribution proposed by Zou and He[16] is used here. For the isothermal problems, the density distribution function at the boundary should satisfy the following condition:

$$f_\alpha^{\mathrm{neq,\,iso}} = f_\beta^{\mathrm{neq,iso}} \,, \tag{23}$$

here e_α and e_β have opposite directions. For the thermal problems, the internal energy density distribution function at the boundary satisfies:

$$g_\alpha^{\mathrm{neq}} - e_\alpha^2 f_\alpha^{\mathrm{neq,\,iso}} = -(g_\beta^{\mathrm{neq}} - e_\beta^2 f_\beta^{\mathrm{neq,\,iso}}) \,. \tag{24}$$

Since the density distribution in the thermal model does not take into account the temperature variation, its nonequilibrium part satisfies the boundary condition Eq. (23) and plays the role of $f^{\mathrm{neq,\,iso}}$ in the boundary condition for the internal energy density distribution function. The velocity of the wall is used when f^{eq} for the boundary nodes are calculated in order to enforce the no-slip boundary condition. The temperature of the wall is also used when g^{eq} for the boundary nodes are calculated in order to satisfy the given temperature. For the Neumann type condition, the temperature on the wall is unknown. In order to solve this problem, we transfer it to the Dirichlet type condition by using the conventional second-order finite difference approximation to get the temperature on the boundary. When the heat flux (temperature gradient) is given, the temperature on boundary can be approximated by

$$\left.\frac{\partial T}{\partial y}\right|_{i,1} = \frac{4T_{i,2} - T_{i,3} - 3T_{i,1}}{2\Delta y} \,. \tag{25}$$

The iteration is needed to get accurate values of the temperature on the boundary when Neumann type boundary condition is implemented.

As an example, we consider the case of the bottom wall. The schematic plot of velocity directions of the nine-bit model is shown in Fig. 3. The density distribution function and energy density distribution function at directions 7, 4, and 8 are determined by the calculation using Eqs. (18) and (19). The rest distributions at directions 5, 2, and 6 are determined by the bounce back rule for the nonequilibrium distribution function through Eqs. (23) and (24). Using Eq. (25), the temperature on the bottom wall is updated by

$$T_{i,1} = \frac{4}{3}T_{i,2} - \frac{1}{3}T_{i,3}\,. \tag{26}$$

At corner points, special treatment is needed. Take the bottom-left corner point as an example, which is shown in Fig. 4. For the directions 6 and 8, the values for these two directions have little influence on the results of the numerical simulation using the standard LBM, because they do not contribute any information into the interior parts. But for the TLLBM, these values will be used when calculating the interior points at these two directions. So the values at these two directions should be given. The second order extrapolation scheme is used in this work to determine these values.

3.3. *Nonuniform grid and convergence criterion*

The nonuniform grid is used in the present simulation. A typical nonuniform grid is shown in Fig. 5. It can be seen clearly from Fig. 5 that mesh points are stretched near the wall to capture the thin boundary layer. In the middle part of the flow

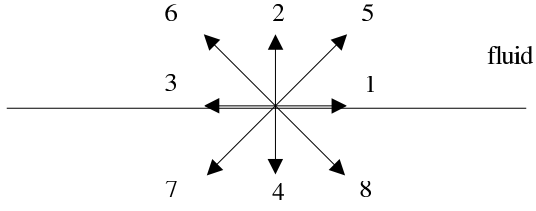

Fig. 3. Schematic plot of velocity directions at the bottom wall.

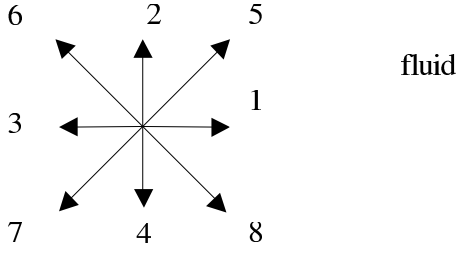

Fig. 4. Schematic plot of velocity directions at bottom-left corner.

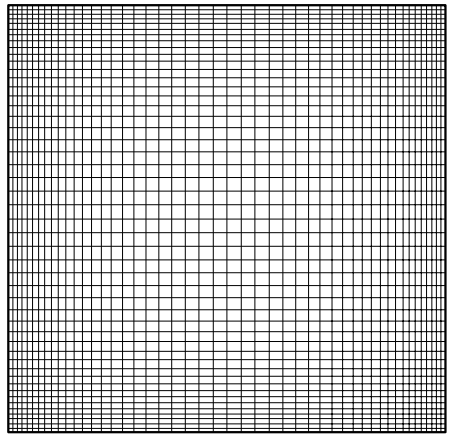

Fig. 5. A Typical nonuniform mesh in a square cavity.

field, the mesh is relatively coarse since the velocity and temperature gradients are not very large in this region.

The convergence criterion for all the cases is set to

$$\max \sum_{i,j} |\sqrt{(u_{i,j}^2 + \nu_{i,j}^2)^{n+1}} - \sqrt{(u_{i,j}^2 + \nu_{i,j}^2)^n}| \leq 10^{-8}\,,$$
$$\max \sum_{i,j} |T^{n+1} - T^n| \leq 10^{-8}\,, \tag{27}$$

where n and $n+1$ represent the old and new time levels.

4. Results and Discussion

4.1. *Validation of the numerical results and analysis of flow and thermal fields*

Table 1 shows the numerical results of the maximum horizontal velocity on the vertical mid-plane of the cavity, $u_{\max}$, and its location Y, the maximum vertical velocity on the horizontal mid-plane of the cavity, $\nu_{\max}$, and its location X, the average Nusselt number throughout the cavity $\overline{\mathrm{Nu}}$ for a wide range of Rayleigh numbers. Note that all the results are computed on the nonuniform grids. The numerical results of Navier–Stokes equations given by Shu and Xue[17] using the DQ method are also included for comparison.

From Table 1, we can see that the numerical results obtained by TLLBM generally agree well with the benchmark results of Shu and Xue in a wide range of Rayleigh numbers. The deviation of the two results at high Rayleigh number is larger than that at low Rayleigh number. The reason may be due to the fact that at high Rayleigh number, the temperature variation is very large, and in the IEDDF thermal model, the mean temperature is used as the reference temperature. Another reason may be that at high Rayleigh number, when the flow becomes weakly

Table 1. Comparison of numerical results between TLLBM and a Navier–Stokes solver.

Rayleigh number	10^3		10^4		10^5		10^6	
Method	TLLBM	DQ	TLLBM	DQ	TLLBM	DQ	TLLBM	DQ
Grid size	51×51	—	101×101	—	151×151	—	201×201	—
$u_{\max}$	3.646	3.649	16.158	16.190	34.301	34.736	63.590	64.775
Y	0.814	0.815	0.824	0.825	0.852	0.855	0.844	0.850
$v_{\max}$	3.694	3.698	19.676	19.638	68.188	68.640	218.32	220.64
X	0.180	0.180	0.121	0.120	0.065	0.065	0.037	0.035
$\overline{\mathrm{Nu}}$	1.117	1.118	2.244	2.245	4.520	4.523	8.804	8.800
$\lvert\Psi_{\mathrm{mid}}\rvert$	1.175	1.175	5.071	5.075	9.104	9.117	16.313	16.270

turbulent, the solution given by the Boussinesq approximation deviates gradually from the true solution. This means that the Boussinesq approximation may not properly describe the flow behavior under realistic temperature conditions beyond a certain Rayleigh number.[18]

With increase of the Rayleigh number, the $u_{\max}$, $\nu_{\max}$, $\overline{\mathrm{Nu}}$ are greatly increased, and the position of maximum vertical velocity on the horizontal mid-plane moves closer to the wall. This can be explained by the following fact. The higher the Rayleigh number, the larger the temperature difference. Since it is a buoyancy driven flow, the buoyancy becomes stronger with the larger temperature difference, and the fluid motion becomes stronger, which can be seen from the larger value of $u_{\max}$, $\nu_{\max}$. Most of the fluid near the wall is driven into the motion and the heat transfer ability increases, leading to the smaller value of X and larger value of $\overline{\mathrm{Nu}}$.

It was found that the Nusselt number obtained by the present LBM is slightly smaller than the Navier–Stokes result of Shu and Xue. This phenomenon has also been observed in the simulation of the Rayleigh–Benard convection by He *et al.*[14] The reason may due to the fact that the macroscopic equation of the LBM is equivalent to the Navier–Stokes equations only up to the second-order of the macroscopic flow velocity. The higher order terms in the expanded Maxwell–Boltzmann equilibrium distribution function are truncated by the so-called low-Mach number approximation. The higher order terms that have not been considered in the macroscopic equations of LBM are no longer negligible in the high Rayleigh number case.

Figures 6 and 7 show the streamlines and isotherms of $\mathrm{Ra} = 10^3$, 10^4, 10^5, 10^6. These plots agree well with those obtained by Shu and Xue. Hot fluids near the left wall flow upward to the right wall and the temperature of the fluids are decreased, while cold fluids near the right wall flow downward to the left wall and the temperature of the fluids are increased. When the Rayleigh number increases, the mixture of the hot and the cold fluids is enhanced and the temperature gradients near the left and right walls are increased, meaning the enhancement of the heat transfer within the square cavity. This leads to the increase of the stream function value Ψ and Nusselt number Nu, which can also be seen in Table 1.

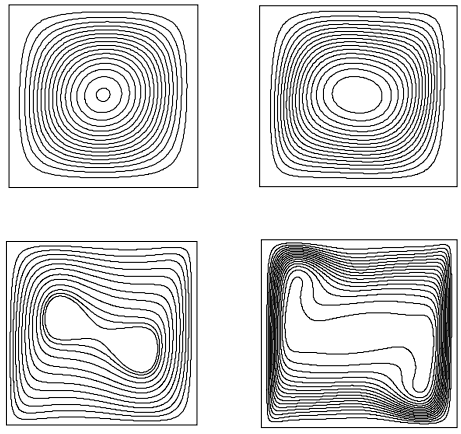

Fig. 6. Streamlines of $\mathrm{Ra} = 10^3$, 10^4, 10^5 and 10^6.

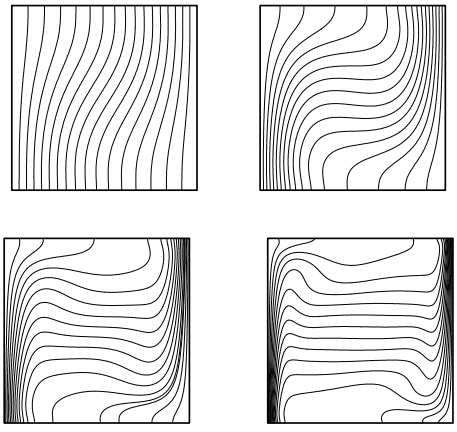

Fig. 7. Isotherms of $\mathrm{Ra} = 10^3$, 10^4, 10^5 and 10^6.

4.2. *Comparison of numerical results on uniform and nonuniform grids*

In order to see the efficiency of using the nonuniform grids, the numerical simulations for the same Rayleigh number on uniform and nonuniform grids were carried out. Tables 2–5 show the comparison of the numerical results on two different grids for Rayleigh numbers of 10^3, 10^4, 10^5, 10^6.

It can be observed from Tables 2–5 that, for the same Rayleigh number and the same number of grid points, the calculated Nusselt number on the nonuniform grid is more accurate than that on the uniform grid. For example, as can be seen from Table 2, for Rayleigh number of 10^3, the calculated $\overline{\mathrm{Nu}}$ and $\mathrm{Nu}_{1/2}$ on the nonuniform grid of 51×51 are 1.117 and 1.118, while the calculated $\overline{\mathrm{Nu}}$ and $\mathrm{Nu}_{1/2}$ on the uniform grid of 51×51 are only 1.116 and 1.114. When the grid size of the

Table 2. Comparison of numerical results on uniform and nonuniform grids for $\mathrm{Ra} = 10^3$.

Mesh	51×51 (uniform)	101×101 (uniform)	51×51 (nonuniform)	DQ
$\lvert\Psi_{\mathrm{mid}}\rvert$	1.170	1.175	1.175	1.175
$u_{\max}$	3.636	3.649	3.646	3.649
Y	0.820	0.810	0.814	0.815
$v_{\max}$	3.702	3.700	3.694	3.698
X	0.180	0.180	0.180	0.180
$\overline{\mathrm{Nu}}$	1.116	1.117	1.117	1.118
$\mathrm{Nu}_{1/2}$	1.114	1.116	1.118	1.118

Table 3. Comparison of numerical results on uniform and nonuniform grids for $\mathrm{Ra} = 10^4$.

Mesh	101×101 (uniform)	151×151 (uniform)	101×101 (nonuniform)	DQ
$\lvert\Psi_{\mathrm{mid}}\rvert$	5.063	5.069	5.071	5.075
$u_{\max}$	16.158	16.156	16.158	16.190
Y	0.820	0.820	0.824	0.825
$v_{\max}$	19.704	19.679	19.676	19.638
X	0.120	0.120	0.121	0.120
$\overline{\mathrm{Nu}}$	2.232	2.237	2.244	2.245
$\mathrm{Nu}_{1/2}$	2.224	2.231	2.244	2.245

Table 4. Comparison of numerical results on uniform and nonuniform grids for $\mathrm{Ra} = 10^5$.

Mesh	151×151 (uniform)	201×201 (uniform)	151×151 (nonuniform)	DQ
$\lvert\Psi_{\mathrm{mid}}\rvert$	9.102	9.103	9.104	9.117
$\lvert\Psi_{\max}\rvert$	9.648	9.644	9.631	9.618
X	0.287	0.285	0.287	0.285
Y	0.607	0.605	0.606	0.600
$u_{\max}$	34.194	34.245	34.301	34.736
Y	0.853	0.855	0.852	0.855
$v_{\max}$	68.282	68.276	68.188	68.640
X	0.067	0.065	0.065	0.065
$\overline{\mathrm{Nu}}$	4.494	4.501	4.520	4.523
$\mathrm{Nu}_{1/2}$	4.487	4.496	4.518	4.524

uniform grid is increased to 101×101, the calculated $\overline{\mathrm{Nu}}$ and $\mathrm{Nu}_{1/2}$ then become 1.117 and 1.116. As compared with the benchmark data of $\overline{\mathrm{Nu}}$ and $\mathrm{Nu}_{1/2}$ which are 1.118 and 1.118, it is clear that the use of mesh size of 51×51 on the nonuniform grid gives much better results than the use of same mesh size on the uniform grid. Even when more mesh points are used on the uniform grid, the nonuniform grid

Table 5. Comparison of numerical results on uniform and non-uniform grids for $\mathrm{Ra} = 10^6$.

Mesh	201×201 (uniform)	251×251 (uniform)	201×201 (nonuniform)	DQ
$\lvert\Psi_{\mathrm{mid}}\rvert$	16.359	16.369	16.313	16.270
$\lvert\Psi_{\max}\rvert$	16.832	16.827	16.815	16.714
X	0.150	0.148	0.150	0.150
Y	0.555	0.552	0.560	0.550
$u_{\max}$	63.251	63.527	63.590	64.775
Y	0.840	0.844	0.844	0.850
$v_{\max}$	218.33	218.47	218.32	220.64
X	0.040	0.040	0.037	0.035
$\overline{\mathrm{Nu}}$	8.766	8.781	8.804	8.800
$\mathrm{Nu}_{1/2}$	8.759	8.775	8.803	8.799

still gives better results. This is because when a nonuniform grid is used, it is easy for us to use very small mesh spacings near the boundary to capture the thin boundary layer. In contrast, when the same mesh spacing is used by the uniform grid to capture the thin boundary layer, the number of mesh points used in the whole flow field could be very large. This example clearly shows the advantages of using a nonuniform grid in the simulation of flow problems.

As far as the computational efficiency is concerned, for the same grid number, the calculation time on the nonuniform grid using TLLBM is more than that on the uniform grid using standard LBM. But it will take much less grid numbers for the nonuniform grid to get the same accurate results. The combining result of these two effects is that it will take less computation time for TLLBM to get the results at the same accuracy. Take $\mathrm{Ra} = 10^3$ as an example. All the computation is done on PCIII 1.6 G. It will take 87.30 s to get the convergent result on the uniform grid with the mesh size of 51×51 using standard LBM, while it will take 242.85 s on the nonuniform grid for the same grid size using TLLBM. But as shown above, compared with the benchmark data, the grid size of the uniform grid should be increased to 101×101 to get the accurate result, while the use of mesh size of 51×51 on the nonuniform grid can give much better results. The calculation time for the uniform grid with mesh size of 101×101 is 574.25 s. This example shows that TLLBM is more efficient than the standard LBM to get the same accurate results.

5. Conclusions

The explicit TLLBM is applied in this work to simulate the natural convection in a square cavity for Rayleigh number ranging from 10^3 to 10^6 on both uniform and nonuniform grids. The numerical results compare well with the benchmark data obtained by a Navier–Stokes solver. Less grid points are needed to get the accurate results for nonuniform grid. From the present work, it was found that the

present explicit method is an efficient way to extend the current thermal model to practical applications on the nonuniform grid. The extension to the arbitrary grid for the thermal problem with curved boundary is straightforward since the method is basically a mesh-free approach. On the other hand, it still keeps the local and explicit features of the standard LBM and no solution of differential equation is involved in this method.

References

1. X. He, L.-S. Luo, and M. Dembo, *J. Comp. Phys.* **129**, 357 (1996).
2. X. He and G. D. Doolen, *J. Comp. Phys.* **134**, 306 (1997).
3. X. He and G. D. Doolen, *Phys. Rev. E* **56**, 434 (1997).
4. R. Mei and W. Shyy, *J. Comp. Phys.* **134**, 306 (1997).
5. F. Nanelli and S. Succi, *J. Stat. Phys.* **68**, 401 (1992).
6. G. Peng, H. Xi, and S. H. Chou, *Int. J. Mod. Phys. C* **10**, 1003 (1999).
7. G. Peng, H. Xi, C. Duncan, and S. H. Chou, *Phys. Rev. E* **59**, 4675 (1999).
8. Y. T. Chew, C. Shu, and X. D. Niu, *J. Stat. Phys.* **107**, 329 (2002).
9. C. Shu, Y. T. Chew, and X. D. Niu, *Phy. Rev. E* **64**, 045701 (2001).
10. F. J. Alexander, S. Chen, and J. D. Sterling, *Phy. Rev. E* **47**, R2249 (1993).
11. Y. Chen, H. Ohashi, and M. Akiyama, *Phy. Rev. E* **50**, 2776 (1994).
12. C. Teixeira, H. Chen, and D. M. Freed, *Comp. Phy. Commun.* **129**, 207 (2000).
13. X. Shan, *Phy. Rev. E* **55**, 2780 (1997).
14. X. He, S. Chen, and G. D. Doolen, *J. Comput. Phys.* **146**, 282 (1998).
15. T. Ihle and D. M. Kroll, *Comp. Phys. Commun.* **129**, 1 (2000).
16. Q. Zou and X. He, *Phys. Fluids* **9**, 1591 (1997).
17. C. Shu and H. Xue, *Int. J. Heat & Fluid Flow* **19**, 59 (1998).
18. H. Mlaouah, T. Tsuji, and Y. Nagano, *Int. J. Heat & Fluid Flow* **18**, 100 (1996).